International Journal of Solids and Structures 49 (2012) 3573–3581

Contents lists available at SciVerse ScienceDirect

International Journal of Solids and Structures

journal homepage: www.elsevier.com/locate/ijsolstr

Simulation of earing behaviors in bake hardening steel exhibiting a strong off-γ-fiber component

Eun-Young Kim [a], Shi-Hoon Choi [a,*], Eun-Joo Shin [b], JeongWhan Yoon [c]

[a] Department of Materials Science and Metallurgical Engineering, Sunchon National University, Jeonnam 540-742, Republic of Korea
[b] Korea Atomic Energy Research Institute, Neutron Physics Department, Daejeon 305-600, Republic of Korea
[c] Faculty of Engineering and Industrial Sciences, Swinburne University of Technology, P.O. Box 218, Hawthorn, VIC 3122, Australia

ARTICLE INFO

Article history:
Available online 7 March 2012

Keywords:
Crystal plasticity FEM
Earing
Macrotexture
r-value

ABSTRACT

Analytical theory and a crystal plasticity finite element method (CPFEM) were used to simulate the earing profiles of drawn cups of bake hardening (BH) steel. The two approaches successfully predicted the earing profiles. To analyze the effects of major texture components on earing, orientation distribution functions (ODFs) for 2 γ-fiber ({1 1 1}<1 1 0>, {1 1 1}<1 1 2>) and 1 off-γ-fiber ({5 5 4}<2 2 5>) texture components were calculated using Gaussian standard functions. The proposed two approaches capture the individual contributions of major texture components on the earing profiles of BH steel.

1. Introduction

Bake hardening (BH) steels must have good formability during the press-forming operation and additional hardening from the paint-baking treatment of formed auto-body parts (Baker et al., 2002; Jeong, 2007; Kim et al., 2009). Anisotropic properties, such as the *r*-value (plastic strain ratio) and yield stress affect the formability of BH steels containing extra low carbon (Ray et al., 1994; Bleck et al., 1998; Nakamachi et al., 2001). A dominant metallurgical parameter that influences the anisotropic properties of steel sheet metal is the crystallographic texture (Senuma and Kawasaki, 1994; Choi and Chung, 2002).

The finite element method (FEM) is one of the most powerful tools in the automotive industry for designing new parts (Dawson et al., 2003). However, for the analysis and design of specific materials, FEM users need appropriate data and constitutive models. For the FEM of forming operations, the yield surface and the stress–strain curve provide important material property data. Constitutive equations that are used to describe the plastic yielding of anisotropic materials are divided into two approaches: phenomenological and crystallographic. In the phenomenological approach, the plastic behavior of metals is assumed to be adequately described by yield function. A non-quadratic yield function that describes plastic anisotropy of polycrystalline materials for aluminum alloys was proposed by Barlat et al. (2003, 2005). In the crystallographic approach (Dawson, 2000; Choi et al., 2009; Inal et al., 2000; Raabe and Roters, 2004), the material is assumed to be a polycrystal consisting of many individual crystals (grains). Plastic flow is assumed to occur only by crystallographic slip on given slip systems with each crystal. This approach can be used to take crystallographic texture evolution into account during plastic deformation.

Inal et al. (2000) simulated earing behavior for aluminum alloys using the CPFEM with a model involving only the flange part. The texture component CPFEM has been applied to investigate the influence of major texture components and their combination on the earing behavior of cup drawn polycrystalline FCC (Raabe and Roters, 2004; Zhao et al., 2004; Tikhovskiy et al., 2007) and BCC (Tikhovskiy et al., 2008; Raabe et al., 2005) materials. The studies found that the ear height and profile can be minimized by an optimized combination of major texture components. In the orientation mapping, first, the discrete center orientations, including their scatter width, are extracted by the best fit of the experimental pole figures to the recalculated pole figures. An extracted discrete center orientation is assigned to each integration point. The assigned discrete center orientations are systematically re-oriented to the neighboring integration points. The orientation mapping scheme requires additional modification of the fitted random background to fit experimental earing profiles (Raabe and Roters, 2004).

In the present work, earing profiles during the cup-drawing of BH steels were investigated using an analytical theory (Yoon et al., 2011) and a crystal plasticity finite element method (CPFEM) (Choi et al., 2009). A new orientation mapping scheme based on misorientation was suggested to improve the predictability of earing profiles. A Gaussian standard function was used to generate texture components that are typical in annealed BH steel. Here, the individual effects of major texture components that are typical for BH steel on earing profiles are discussed systematically.

* Corresponding author. Tel.: +82 61 750 3556; fax: +82 61 750 3550.
E-mail address: shihoon@sunchon.ac.kr (S.-H. Choi).

0020-7683/$ - see front matter © 2012 Elsevier Ltd. All rights reserved.
http://dx.doi.org/10.1016/j.ijsolstr.2012.02.027

2. Experimental and texture generation

2.1. Experiment

Hot rolling, cold rolling, and annealing conditions all contribute to development of crystallographic texture in BH steels. The major texture component in the hot-rolled BH steel can be characterized by {0 0 1}<1 1 0>, which is transformed from the cube texture component in the austenite region. Cold-rolling deformation simultaneously enhances the intensity of α-fiber (<1 1 0>//RD) and γ-fiber (<1 1 1>//ND) texture components. Annealing decreases the intensity of the α-fiber texture components and increases the intensity of orientation distribution function (ODF) in the γ-fiber texture components. The relative intensity of these components strongly depends on the processing conditions and on the material composition.

The macro-texture of annealed BH steel was quantitatively examined using neutron diffraction. The crystallographic textures were determined by measuring the pole figures with a four-circle neutron diffractometer (FCD) using a neutron beam with a wavelength of 1.31 Å. The (1 1 0), (2 0 0), and (2 1 1) complete pole figures were used to calculate 3-D ODF using the WIMV method (Matthies et al., 1988). Fig. 1(a) and (b) show the ODF distribution in 3-D Euler space and the $\varphi_2 = 45°$ section of the annealed BH steel, as observed by neutron diffraction. Texture components typically observed in BH steel are shown in the $\varphi_2 = 45°$ section of ODF. This result reveals that the initial texture of annealed HSS sheets can be characterized as γ-fiber texture and off-γ-fiber texture components (~{5 5 4}<2 2 5>). An ODF determined from a Gaussian standard function was used to generate a set of 1000-grain orientations for polycrystal modeling with the help of orientation repartition functions (Francois et al., 1991).

Tension tests were conducted at room temperature (RT) to measure the *r*-values and yield stresses using a standardized dimension (JIS-5). Tensile specimens were cut from the sheet at angles of 0°, 45°, and 90° from the rolling direction (RD). Fig. 2 shows the experimental true stress–true strain curves for the annealed BH steel. The experimental data measured at 15% elongation are as follows:

$$\sigma_0 = 404.8 \text{ MPa};\ \sigma_{45} = 421.5 \text{ MPa};\ \sigma_{90} = 401.9 \text{ MPa};$$
$$r_0 = 1.61;\ r_{45} = 1.04;\ r_{90} = 1.81.$$

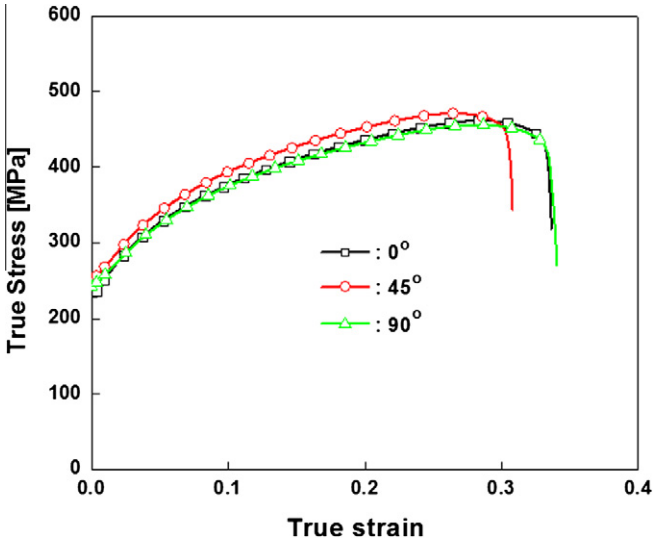

Fig. 2. Experimental true stress-true strain curves for the annealed BH steel.

In the actual cup-drawing process, 80 mm diameter blanks (initial thickness 0.7 mm) were drawn into a 40 mm-diameter cup using a drawing ratio of 2.0. The specific dimensions of the tools for the cup-drawing process were as follows:

- Punch radius (R_p) = 20 mm;
- Punch profile radius (r_p) = 6 mm;
- Die profile radius (r_d) = 8 mm;
- Blank radius (R_b) = 40 mm; and,
- Blank holding force was 1TonF.

2.2. Generation of major texture components

To analyze the effects of major texture components on earing behaviors, 2 γ-fiber ({1 1 1}<1 1 0>, {1 1 1}<1 1 2>) and 1 off-γ-fiber ({5 5 4}<2 2 5>) texture components were selected. ODF around a single ideal component can be mathematically described using the "Gaussian standard function" (Matthies et al., 1987–1990)

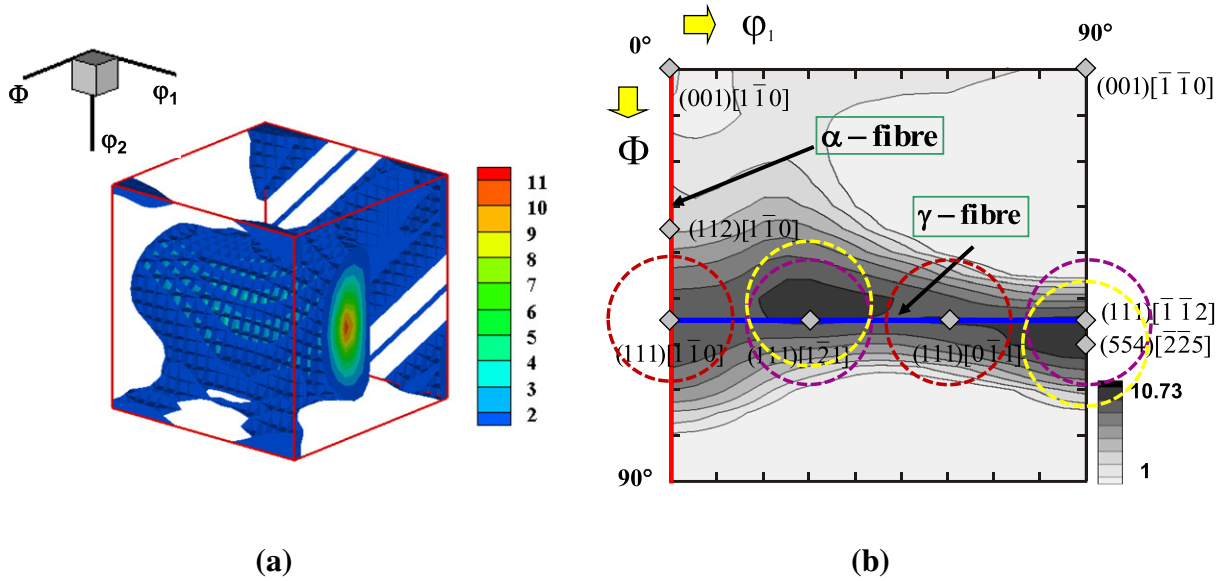

Fig. 1. (a) ODF distribution in 3-D Euler space and (b) $\varphi_2 = 45°$ section of the annealed BH steel as observed by neutron diffraction.

$$f(S,\tilde{\omega}) = N(S)e^{S\cos\tilde{\omega}}, \quad N(S) = 1/(I_0(S) - I_1(S)),$$
$$I_k(x) = \tfrac{1}{\pi}\int_0^{\pi} e^{x\cos t}\cos kt\,dt, \qquad (1)$$
$$S = \ln 2/[2\sin^2(b/4)] \quad \text{for } b \leqslant 2\pi.$$

where $f(S,\tilde{\omega})$ expresses the relative density of an orientation g rotated through an orientation distance $\tilde{\omega} = \tilde{\omega}(g_k^o, g)$ from the single ideal orientation g_k^o. b (=1.665ω; ω = Bunge's notation) and $I_k(x)$ are the half-width (FWHM-[full-width at half-maximum]) of the bell-shaped curve and the modified Bessel function, respectively. A value of $b = 25^\circ$ was selected as the half-width of a bell-shaped Gaussian standard function. The typical texture component of 80% as a volume fraction was generated with a random background component of 20%. An ODF determined from a Gaussian standard function was used to generate a set of 1000-grain orientations for polycrystal modeling (Francois et al., 1991).

3. Theoretical procedure

3.1. Analytical theory for earing height

The analytical theory to predict earing height used in the present work (Yoon et al., 2011) is based on two approximations. First, directionalities of the *r*-value and yield stress are the major sources of earing. Second, only flange deformation is considered to calculate cup height profile. By using the stress equilibrium and kinematics at the inner most radius and the rim parts, the total height of a deep-drawn cup can be obtained as a function of die geometry and anisotropic properties as follows (Yoon et al., 2011):

$$H^{\text{cup}}(\theta) = t_o + r_p + \frac{R_b}{\frac{r_{\theta+90}}{1+r_{\theta+90}}+1}\left(\left(\frac{R_b}{R_p}\right)^{\frac{r_{\theta+90}}{1+r_{\theta+90}}} - \frac{1}{R_b/R_p}\right)\left(\left(\frac{\sigma_{\text{ref}}}{\sigma^Y_{(\theta)}}\right)^{\beta}\right)^{\frac{r_{\theta+90}}{1+r_{\theta+90}}}, \qquad (2)$$

where

$$\sigma_{\text{ref}} = \left(\int_0^{2\pi}\sigma^Y_{(\theta)}\,d\theta\right)\Big/2\pi = (1/12)(\sigma_0 + 2(\sigma_{15}+\sigma_{30}+\sigma_{45}+\sigma_{60}+\sigma_{75}) + \sigma_{90}).$$

It is of further interest to derive the specific contributions of *r*-value directionality, r_θ, and yield stress directionality, σ_θ, to the cup height. For this purpose, an isotropic contribution can be derived using $r_{\theta+90} = 1$ and $\frac{\sigma_{\text{ref}}}{\sigma^Y_{(\theta)}} = 1$ as

$$H^{iso} = t_o + r_p + \frac{R_b}{1.5}\left(\left(\frac{R_b}{R_p}\right)^{0.5} - \frac{1}{R_b/R_p}\right). \qquad (3)$$

The cup height only from *r*-value directionality is obtained by excluding the yield stress contribution with the assumption that $\frac{\sigma_{\text{ref}}}{\sigma^Y_{(\theta)}} = 1$, i.e.,

$$H^{\text{r-value}}(\theta) = t_o + r_p + \frac{R_b}{\frac{r_{\theta+90}}{1+r_{\theta+90}}+1}\left(\left(\frac{R_b}{R_p}\right)^{\frac{r_{\theta+90}}{1+r_{\theta+90}}} - \frac{1}{R_b/R_p}\right). \qquad (4)$$

In the same vein, the cup height from yield stress directionality is obtained by using $r_{\theta+90} = 1$, i.e.,

$$H^{\text{stress}}(\theta) = t_o + r_p + \frac{R_b}{1.5}\left(\left(\frac{R_b}{R_p}\right)^{0.5} - \frac{1}{R_b/R_p}\right)\left(\left(\frac{\sigma_{\text{ref}}}{\sigma^Y_{(\theta)}}\right)^{\beta}\right)^{0.5}, \qquad (5)$$

when the stress mode at the inner most flange is applied for the entire flange, $\beta = 1.0$.

Then, the cup height contributions of *r*-value and yield stress directionalities can be derived as follows (Yoon et al., 2011):

$$\Delta H^{\text{r-value}}(\theta) = H^{\text{r-value}}(\theta) - H^{iso} \qquad (6a)$$

and

$$\Delta H^{\text{stress}}(\theta) = H^{\text{stress}}(\theta) - H^{iso} \qquad (6b)$$

3.2. Crystal plasticity FEM

Macroscopic anisotropy and cup-drawing behaviors were simulated using the finite element code, ABAQUS with the material model programmed by a continuum crystal plasticity theory. A rate-dependent constitutive relationship was implemented into the user material subroutine UMAT in ABAQUS (2000). The model was fundamentally based on a multiplicative decomposition of the deformation gradient, F, into a plastic part characterized by shearing rates on an active slip system, as well as a part that accounts for the rotation and elastic distortion of the crystal lattice. This formulation leads to additive decomposition of the velocity gradient into elastic and plastic parts,

$$L = L^e + L^p \qquad (7)$$

with the plastic part determined by slip rates, $\dot{\gamma}^\alpha$, on slip planes with normals, m^α, and slip directions, s^α

$$L^p = \sum_{\alpha=1}^{N}\dot{\gamma}^\alpha s^\alpha \otimes m^\alpha \qquad (8)$$

The summation represents all of the slip systems, *N*. The plastic part of the velocity gradient is decomposed further into symmetric and antisymmetric parts ($L^p = D^p + \omega^p$) to yield the formula

$$D^p = \frac{1}{2}\sum_{\alpha=1}^{N}\dot{\gamma}^\alpha(s^\alpha\otimes m^\alpha + m^\alpha\otimes s^\alpha) = \sum_{\alpha=1}^{N}\dot{\gamma}^\alpha P^\alpha$$
$$\omega^p = \frac{1}{2}\sum_{\alpha=1}^{N}\dot{\gamma}^\alpha(s^\alpha\otimes m^\alpha - m^\alpha\otimes s^\alpha) = \sum_{\alpha=1}^{N}\dot{\gamma}^\alpha W^\alpha \qquad (9)$$

where D^p is the plastic part of the rate of deformation tensor and ω^p is the plastic spin.

As described in Peirce et al. (1983), the Jaumann rate of Kirchhoff stress can be expressed as

$$\hat{\tau} = \mathbf{K} : D - \sum_{\alpha=1}^{N}\dot{\gamma}^\alpha R^\alpha \qquad (10)$$

where *K* is a fourth-order tensor based on the anisotropic elastic modulus, *C*. *D* is the rate of deformation tensor (symmetric part of the velocity gradient), and R^α is a tensor that depends on the current slip plane normal and direction, the applied stress and the elastic modulus. For materials having cubic crystal symmetry, the present work uses three independent elastic constants of pure Fe: C_{11} = 231.4 GPa, C_{12} = 134.7 GPa, and C_{44} = 116.4 GPa.

For rate-dependent materials, shear rates are given explicitly in terms of the resolved shear stress on the active slip system and the shear resistance of the active slip system. For these simulations, this dependence is given in the following formula:

$$\dot{\gamma}^\alpha = \dot{\gamma}_o^\alpha\left|\frac{\tau^\alpha}{\tau_o^\alpha}\right|^{1/m}\text{sign}(\tau^\alpha). \qquad (11)$$

Self- and latent-hardening are readily accounted for by a suitable evolution of the reference τ_o^α values in the constitutive law in Eq. (11). The present work employed a microscopic hardening law (Choi, 2003) for this purpose, as follows:

$$\dot{\tau}_o^\alpha = \sum_{\beta}^{N}H^{\alpha\beta}|\dot{\gamma}^\beta| \quad \alpha,\beta = 1\ldots(N_s+N_t), \qquad H^{\alpha\beta} = q^{\alpha\beta}h_o\left(1 - \frac{\tau_o^\alpha}{\tau_{\text{sat}}}\right)^a \qquad (12)$$

Table 1
Microscopic hardening coefficients used in the CPFEM simulation.

τ_o^α (MPa)	h_o (MPa)	τ_{sat} (MPa)	a
65	2000	225	5

where $H^{\alpha\beta}$ is a hardening matrix that is introduced to account for interaction between the slip systems. $q^{\alpha\beta}$ accounts for the hardening rate of the slip system, α, due to slip activity on the system, β. Here, it is assumed that the self-hardening term (diagonal term of $q^{\alpha\beta}$) equals the latent hardening term (off-diagonal term of $q^{\alpha\beta}$), i.e. ($q^{\alpha\beta} = 1$). The fitting simulation was carried out by varying the CRSS values and microscopic hardening parameters (h_o, τ_{sat} and a) until agreement was achieved between the predicted and the measured uniaxial loading curves. In this study, two slip systems ({1 1 0}<1 1 1>, {1 1 2}<1 1 1>) were considered. CRSS values and microscopic hardening parameters were determined by fitting the experimental stress–strain curve. The set of parameters listed in Table 1 was used in the theoretical simulation. Moreover, a material Jacobian ($\partial\Delta\hat{\tau}/\partial\Delta\varepsilon$) for the implicit method can be obtained from Eq. (10). This is equivalent to the modulus given by Peirce et al. (1983). The stress vector in the UMAT subroutine can be updated by multiplying the material Jacobian by the strain increment.

In order to understand the planar anisotropy of BH steel, the CPFEM simulation was performed using 50 elements ($5 \times 5 \times 2$) with 3-D 8-node brick elements, type C3D8R, as shown in Fig. 3(a). The initial length of the model region is given by $l_o = 3.5$ mm, $w_o = 3.5$ mm, and $t_o = 0.7$ mm. The total true strain for uniaxial tension was $\varepsilon = 0.15$. The boundary condition was applied to the four planes comprising the 3-D mesh, as shown in Fig. 3(a). For the uniaxial tension simulation, prescribed displacements in the RD were imposed on the 2-3-7-6 face. To impose initial orientations of the elements, five orientations selected from the 1000-grain orientations were mapped onto each integration point in the finite element mesh. The present study used two mapping schemes for CPFEM simulation. The first scheme (RM) was a random mapping. Five orientations were randomly selected from 1000-grain orientations that were mapped into each integration point, as shown in Fig. 3(b). The macroscopic response of each continuum material point was obtained from a Taylor-type homogenization assumption. The deformation in each orientation was assumed to be identical to the macroscopic deformation of the respective material point. It was assumed that the macroscopic stress response at each continuum material point would be determined by a volume-average over the total number of grains comprising the respective material point. The second scheme (MM) was based on misorientation comprising five orientations, as shown in Fig. 3(b). First, the single center orientation, g_c was randomly selected from the 1000-grain orientations. Second, the misorientation ($\Delta\theta$, i.e. the minimum misorientation angle) between the remaining orientations was calculated using the following formula:

$$\Delta\theta = \min\left[a\cos\left\{\frac{\mathrm{trace}\,(S_v \cdot (g_2^{-1} \cdot g_1)) - 1}{2}\right\}\right], \tag{13}$$

where S_v is the crystal symmetry operator, and v takes values ranging from 1 to 24 for cubic crystal symmetry. The remaining four orientations were selected sequentially from the orientation exhibiting the lowest misorientation value.

The planar anisotropy calculated using the CPFEM is illustrated in Fig. 4 for BH steel. Fig. 4(a) shows the r-values for BH steel as calculated with the CPFEM in different directions as well as those determined experimentally. The predicted r-values using the two mapping schemes overestimated the experimental data for most of the tensile directions. However, it should be noted that the CPFEM calculations correctly predicted r-value directionality under uniaxial tension. Fig. 4(b) shows the normalized yield stresses calculated with the CPFEM as well as those determined experimentally. The CPFEM calculations exhibited good agreement with the experimental results, and were within the range of experimental errors.

Fig. 5 shows the finite element meshes and the geometry of the tools used in the cup-drawing simulation. Due to the orthorhombic sample symmetry, only a quarter of the blank was used to simulate the cup-drawing process. The FE simulation was performed using 918 elements with 3-dimensional 8-node brick elements, called

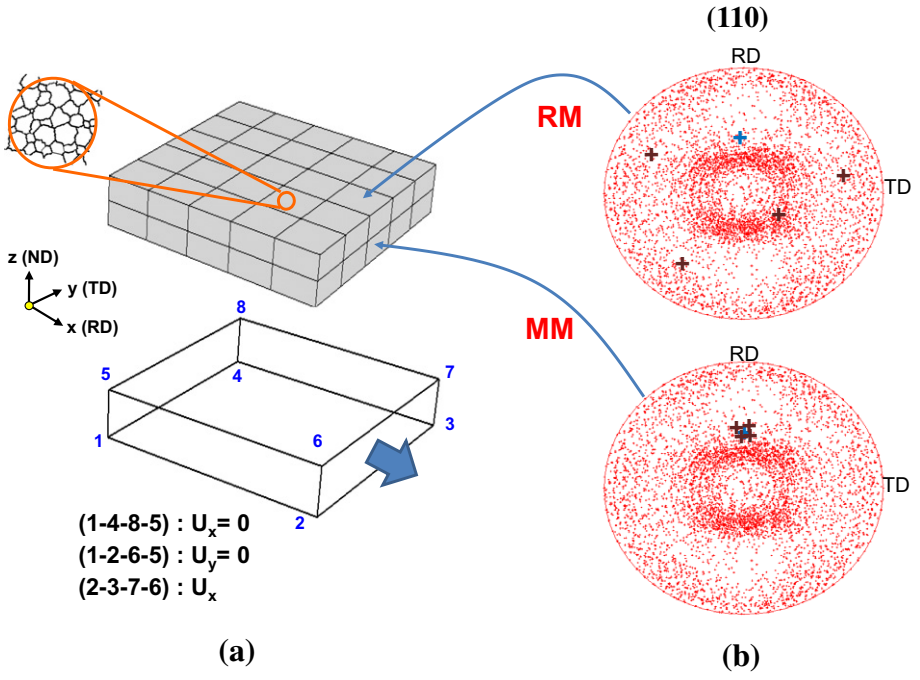

Fig. 3. (a) Finite element mesh and boundary conditions used in the simulation of uniaxial tension and (b) orientation mapping schemes.

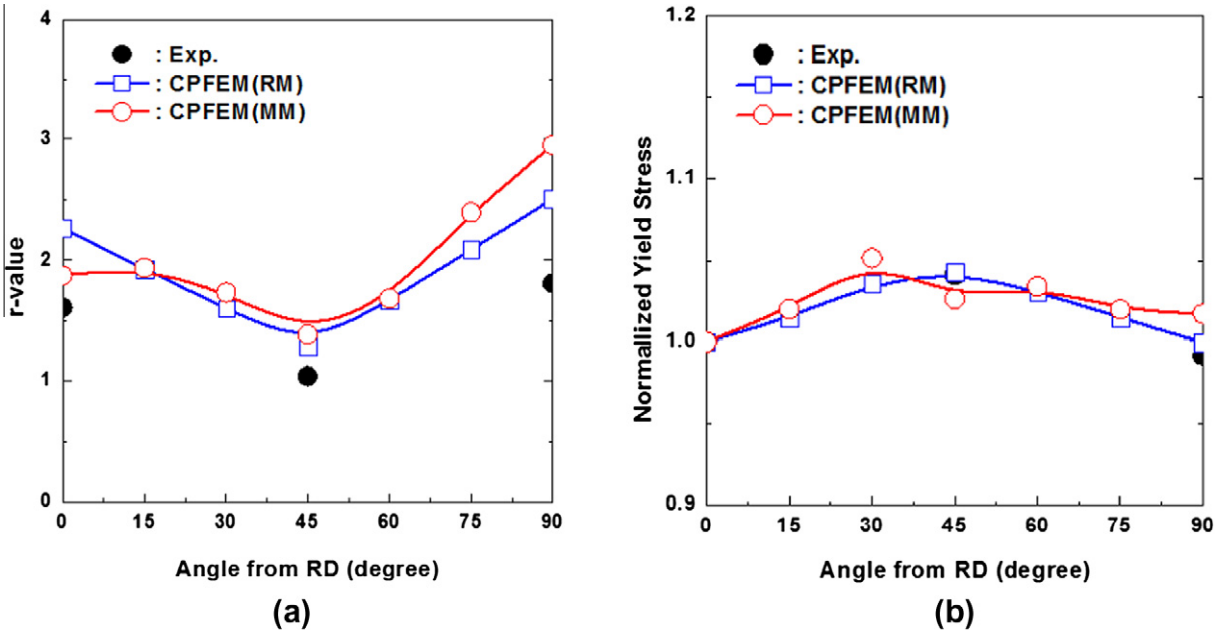

Fig. 4. The planar anisotropy calculated using the CPFEM: (a) *r*-value anisotropy, and (b) normalized yield stress anisotropy.

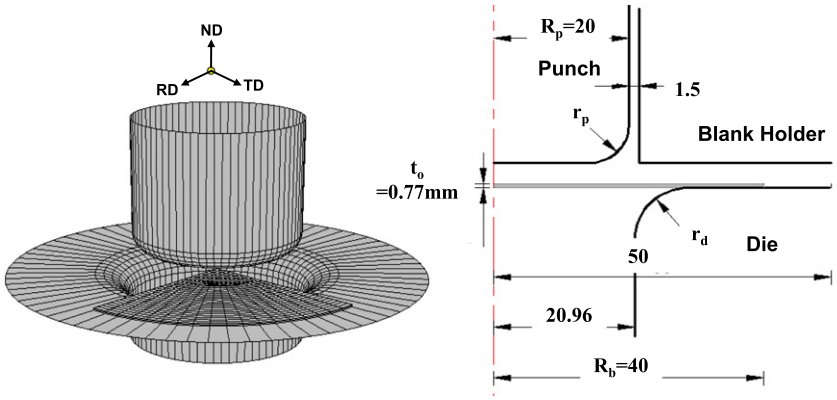

Fig. 5. Finite element meshes and the geometry of the tools used in the cup-drawing simulation.

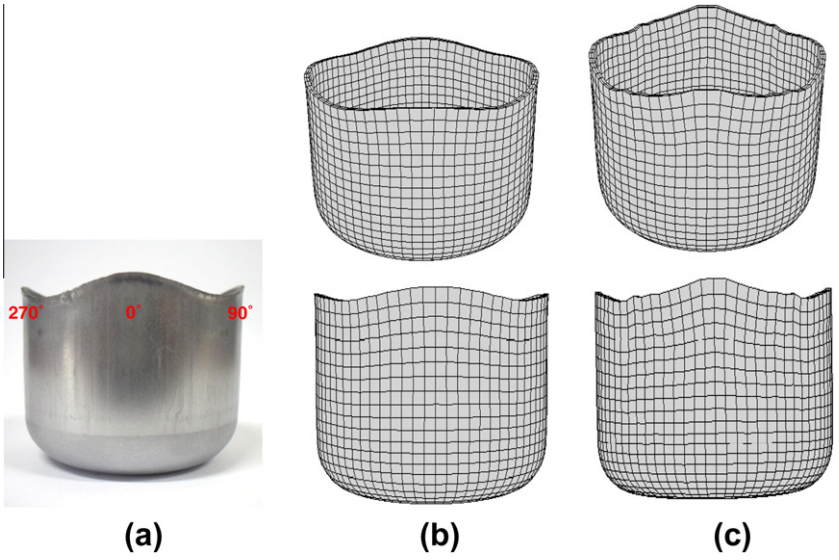

Fig. 6. Cup obtained after cup-drawing process: (a) Experimental, (b) RM, and (c) MM schemes.

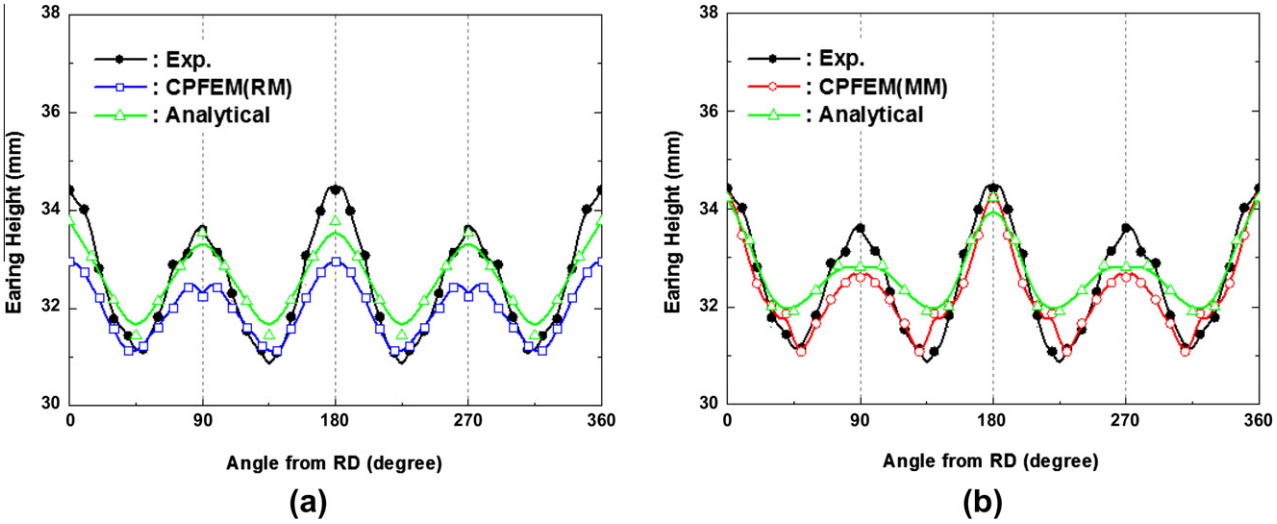

Fig. 7. Earing profiles predicted by the analytical theory: (a) RM, and (b) MM- schemes.

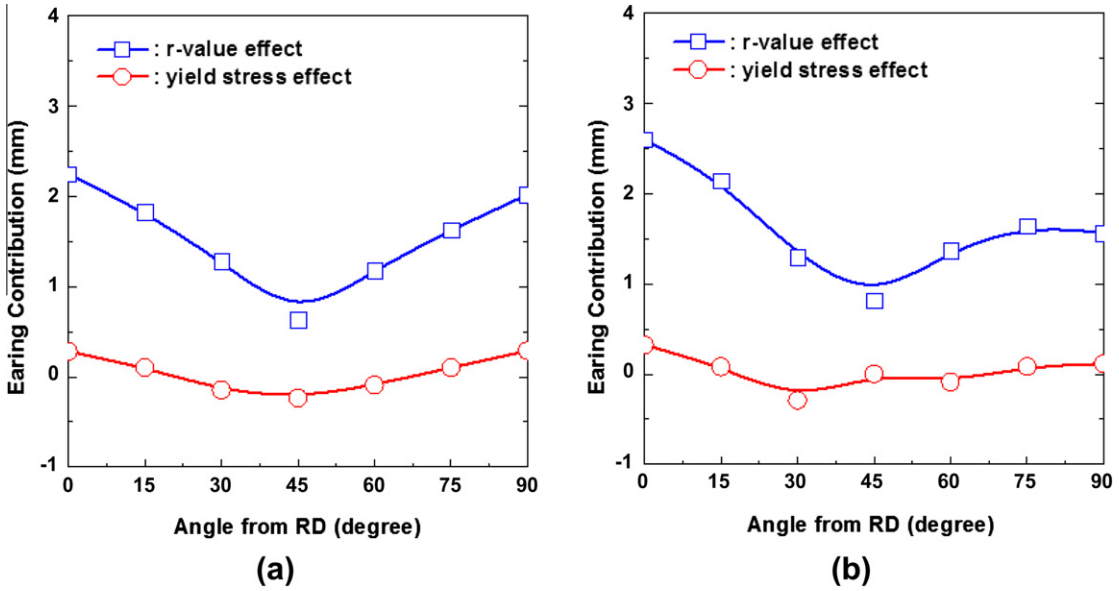

Fig. 8. Cup height contribution to the *r*-value and yield stress directionalities.

C3D8R. The friction coefficient between the blank and the tools was prescribed as $\mu = 0.05$.

4. Results and discussion

Fig. 6(a) shows the cup obtained after the actual cup-drawing process. Fig. 6(b) and (c) show the deformed cups obtained at the final stage of cup-drawing simulation considering RM and MM mapping schemes, respectively. The cup-drawing simulation for the BH steel predicted four ears at approximately 0° and 90° to the RD. Comparisons between the experimental and simulated earing profiles are shown in Fig. 7. The CPFEM results based on an RM mapping scheme underestimated the measured earing profile. Fig. 7 also includes the earing profiles predicted by the analytical theory, as explained in Section 3.1. The calculated directionalities of *r*-value and yield stress, as shown in Fig. 4, were used as the input data for the analytical theory of Eq. (2). As shown in Fig. 7(a), the analytical results based on the directionalities determined by the RM mapping scheme (Fig. 4(a)) produced a similar earing profile with the CPFEM results based on the RM mapping scheme. The earing height determined by the analytical theory was slightly higher than that obtained by the CPFEM. Fig. 7(b) shows a comparison of the CPFEM results based on an MM mapping scheme with the analytical results based on the directionalities determined by the MM mapping scheme (Fig. 4(b)). It should be noted that the analytical results of earing profiles based on the RM mapping scheme were closer to the measured earing profiles than those based on the MM mapping scheme. Contrary to the analytical results, CPFEM results based on the MM mapping scheme produced an earing profile closer to the measured earing profiles, particularly in the region between 0° and 45° from RD.

Fig. 8 shows the cup height contribution of the *r*-value and the yield stress directionalities. The contribution of the *r*-value directionality is larger than that of the stress directionality regardless of mapping schemes. The contributions of the *r*-value and yield-stress directionalities from Eq. (6) correlated directly with those shown in Fig. 4. The earing profile is a scaled mirror image of the *r*-value at 90° from RD in the case of the BH steel.

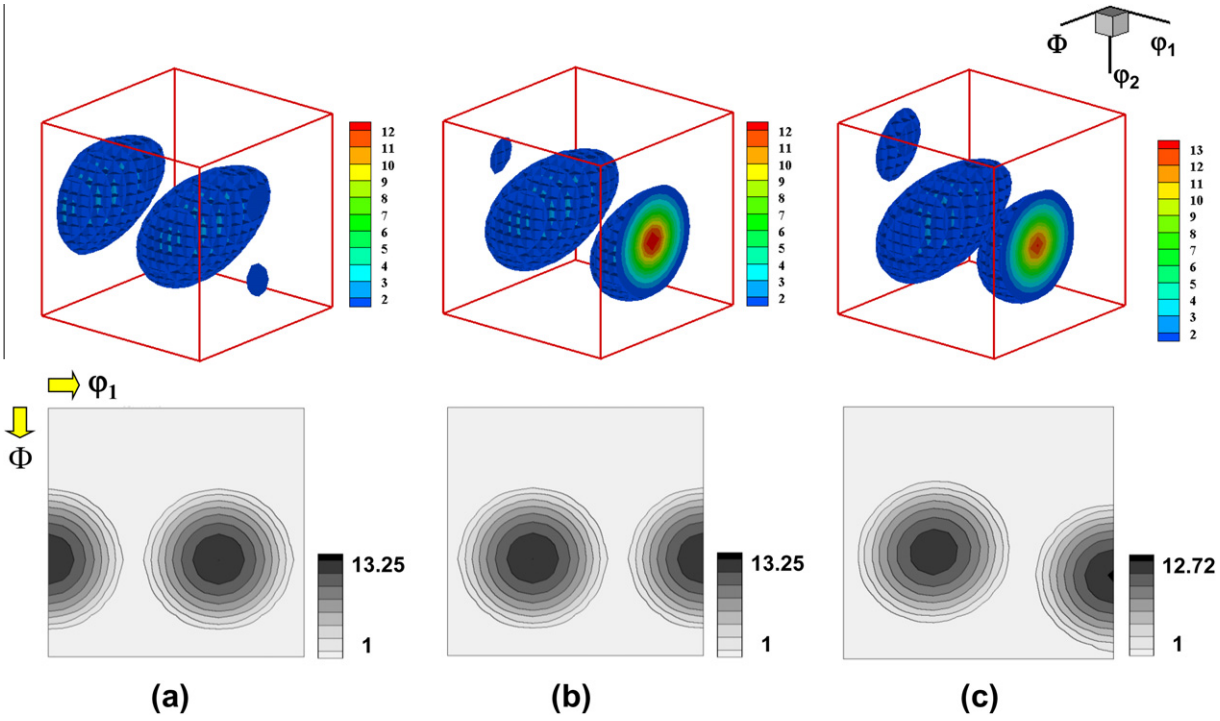

Fig. 9. ODF in 3-D Euler space and $\varphi_2 = 45°$ section of texture components typical in BH steels: (a) {1 1 1}<1 1 0>, (b) {1 1 1}<1 1 2>, (c) {5 5 4}<2 2 5>.

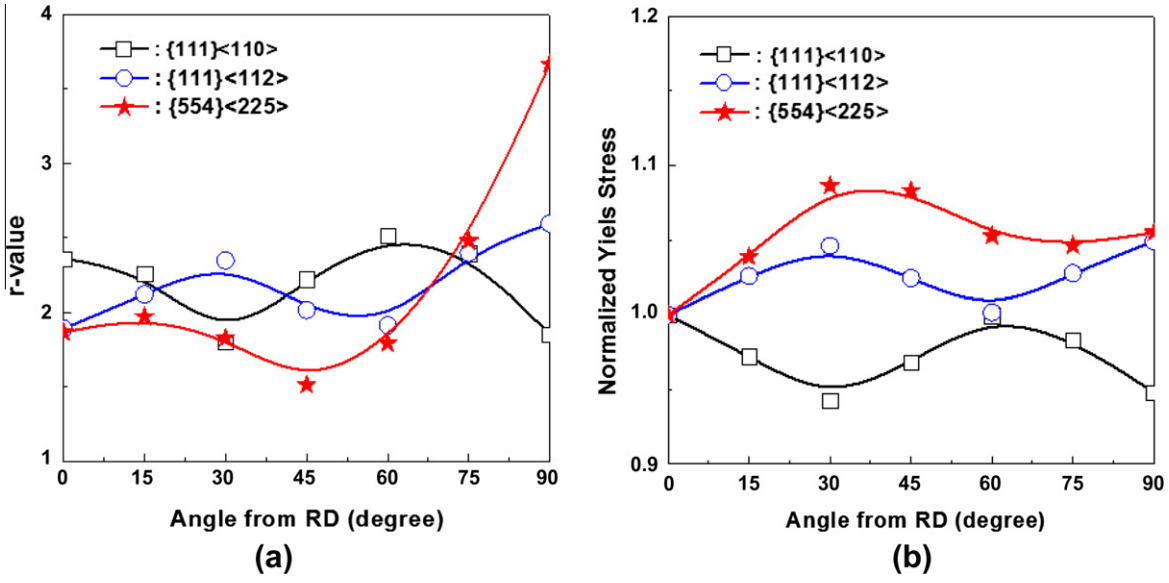

Fig. 10. Planar anisotropy calculated using the CPFEM: (a) *r*-value anisotropy, and (b) normalized yield stress anisotropy.

Fig. 9 shows the ODFs in 3-D Euler space and a $\varphi_2 = 45°$ section of major texture components typical in BH steel. The ODFs were used to generate 1000 discrete orientations for polycrystal modeling. The effects of 2 γ-fiber texture components ({1 1 1}<1 1 0>, {1 1 1}<1 1 2>) and an off-γ-fiber texture component ({5 5 4}<2 2 5>) on planar anisotropy and cup-drawing behaviors was considered. The planar anisotropy for the three typical texture components calculated using the CPFEM is illustrated in Fig. 10. An RM mapping scheme was used for the analytical theory and CPFEM calculations. Fig. 10(a) shows the *r*-value anisotropy for the three texture components calculated using the CPFEM. Fig. 10(b) shows the normalized yield stress anisotropy calculated using the CPFEM. It should be noted that the 2 γ-fiber texture components compensate for the *r*-value and yield stress anisotropy over all loading directions. The *r*-value and yield stress directionalities of the off-γ-fiber texture components were significantly different from the γ-fiber texture component ({1 1 1}<1 1 2>), which had a misorientation of ~5° to the off-γ-fiber texture component. It is clear that the off-γ-fiber texture component exhibited a strong anisotropy for the *r*-value of loading directions between 60° and 90° from the RD. The off-γ-fiber texture component also exhibited a strong anisotropy of yield stress compared to the 2 γ-fiber texture components. Fig. 11 shows a comparison between the earing profiles simulated using the CPFEM and the earing profiles predicted using the analytical theory. The analytical results were qualitatively in good agreement with the CPFEM results. Fig. 12 shows the cup height contribution of the *r*-value and yield stress

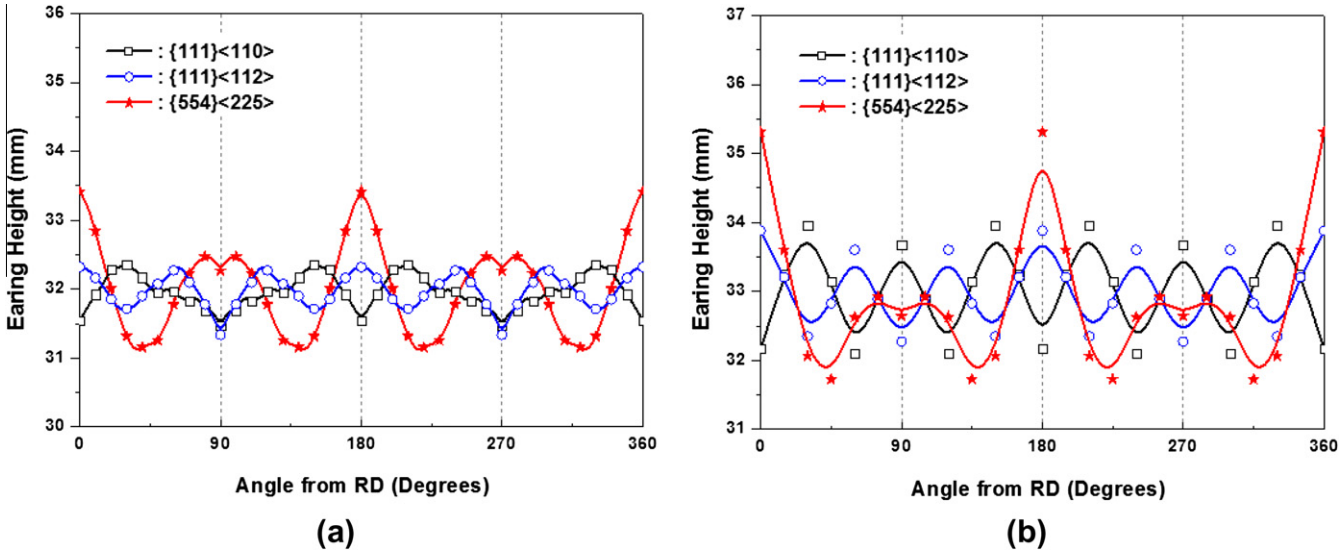

Fig. 11. (a) Earing profiles simulated using the CPFEM, and (b) earing profiles predicted using the analytical theory.

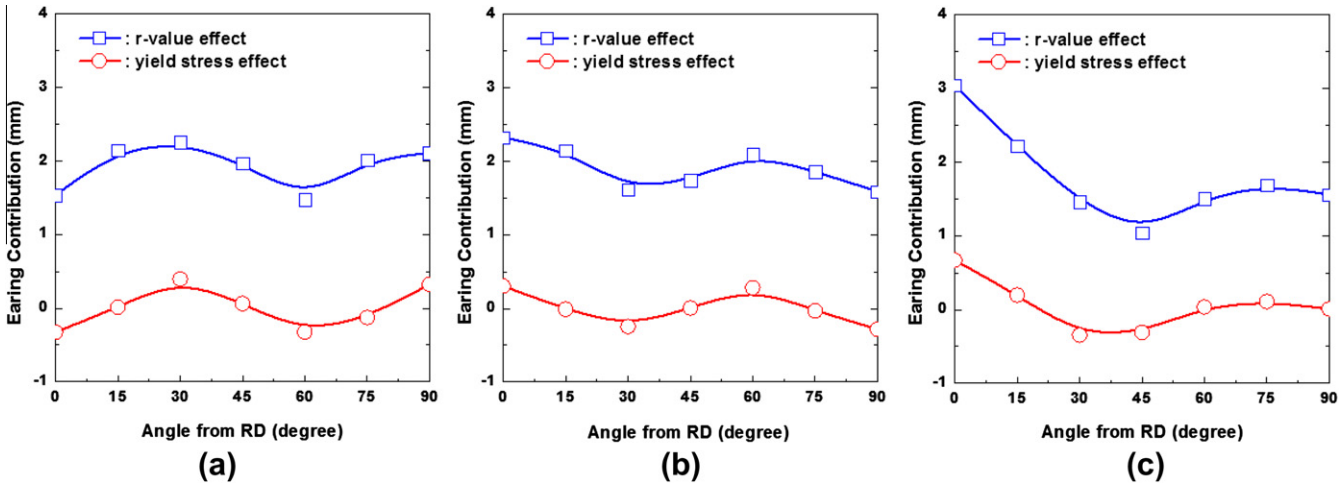

Fig. 12. Cup height contribution of the *r*-value and yield stress directionalities.

directionalities as determined using Eq. (6). Regardless of the texture component, the contribution of the *r*-value directionality was larger than that of the stress directionality. The contributions of *r*-value and yield stress directionalities were directly correlated with those shown in Fig. 4. It is obvious that 2 γ -fiber texture components compensated for the anisotropy of the earing profile over all loading directions. The results showed that the *r*-value directionality of an off-γ-fiber texture component dominantly contributed to the earing profiles of BH steel.

5. Conclusions

The present study predicted the earing profiles during the cup-drawing of BH steel using analytical theory and the crystal plasticity finite element method (CPFEM).

The analytical results based on an RM mapping scheme produced an earing profile closer to the measured earing profiles of BH steel than that based on an MM mapping scheme. However, CPFEM results based on MM mapping produced an earing profile that was closer to the measured earing profiles, particularly in the region between 0° and 45° from RD.

The individual effect of major texture components typical in BH steel on earing profiles was also investigated. Discrete orientations for polycrystal modeling was determined with the help of a "Gaussian standard function" and an "orientation repartition function". The 2 γ-fiber texture components ({1 1 1}<1 1 0>, {1 1 1}<1 1 2>) compensated for the *r*-value and yield-stress directionalities over all loading directions. The off-γ-fiber texture component exhibited a strong anisotropy for the *r*-value of loading directions between 60° and 90° from the RD. The *r*-value directionality of the off-γ-fiber texture component dominantly contributed to the earing profiles of BH steel.

Acknowledgments

This study was supported by a grant from the Nuclear Research & Development Program of the Korea Science and Engineering Foundation (KOSEF) funded by the Korean government (MEST).

References

ABAQUS User's Manual, 2000. version 6.1, Hibbit, Karlsson & Sorenson, Providence, RI.

Baker, L.J., Daniel, S.R., Parker, J.D., 2002. Metallurgy and processing of ultralow carbon bake hardening steels. Materials Science and Technology 18, 355–368.
Barlat, F., Brem, J.C., Yoon, J.W., Chung, K., Dick, R.E., Lege, D.J., Pourboghrat, F., Choi, S.-H., Chu, E., 2003. Plane stress yield function for aluminum alloy sheets-part 1: theory. International Journal of Plasticity 19, 1297–1319.
Barlat, F., Aretz, H., Yoon, J.W., Karabin, M.E., Brem, J.C., Dick, R.E., 2005. Linear transformation-based anisotropic yield functions. International Journal of Plasticity 21, 1009–1039.
Bleck, W., Deng, Z., Papamantellos, K., Oliver Gusek, C., 1998. A comparative study of the forming-limit diagram models for sheet steels. Journal of Materials Processing Technology 83, 223–230.
Choi, S-H., 2003. Simulation of stored energy and orientation gradients in cold-rolled interstitial free steels. Acta Materialia 51, 1775–1788.
Choi, S.-H., Chung, J.H., 2002. Effect of carbon on the *r*-value anisotropy in Ti-added high strength IF steels. Journal of Korean Institute of Metals & Materials 40, 260–265.
Choi, S.-H., Han, S.H., Chin, K.G., 2009. Simulation of orientation gradients in a ferrite matrix containing hard martensite under plane-strain flange deformation. Acta Materialia 51, 1947–1958.
Dawson, P.R., 2000. Computational crystal plasticity. International Journal of Solids and Structures 37, 115–130.
Dawson, P.R., MacEwen, S.R., Wu, P-D., 2003. Advances in sheet metal forming analyses: dealing with mechanical anisotropy from crystallographic texture. International Materials Reviews 48, 86–122.
Francois, M., Sprauel, J.M., Lebrun, J.L., 1991. Construction of a pseudo-material representation of a real textured material from ODF or direct pole figures. Textures Microstructures 14–18, 169–174.
Inal, K., Wu, P.D., Neale, K.W., 2000. Simulation of earing in textured aluminum sheets. International Journal of Plasticity 16, 635–648.
Jeong, W.C., 2007. Relationship between mechanical properties and microstructure in a 1.5% Mn–0.3% Mo ultra-low carbon steel with bake hardening. Materials Letters 61, 2579–2583.
Kim, S.I., Chin, K.G., Yoon, J.B., 2009. Precipitation hardening with copper sulfide in Cu bearing extra low carbon steel sheet. ISIJ International 49, 109–114.
Matthies, S., Vinel, G.W., Helming, K., 1987–1990. Standard Distributions in Texture Analysis, vol. I–III. Akademie Verlag, Berlin, Germany.
Matthies, S., Wenk, H.-R., Vinel, G.W., 1988. Some basic concepts of texture analysis and comparison of three methods to calculate orientation distributions from pole figures. Journal of Applied Crystallography 21, 285–304.
Nakamachi, E., Xie, C.L., Harimoto, M., 2001. Drawability assessment of BCC steel sheet by using elastic/crystalline viscoplastic finite element analyses. International Journal of Mechanical Sciences 43, 631–652.
Peirce, D., Asaro, R.J., Needleman, A., 1983. Material rate dependence and localized deformation in crystalline solids. Acta Metallurgica 31, 1951–1976.
Raabe, D., Roters, F., 2004. Using texture components in crystal plasticity finite element simulations. International Journal of Plasticity 20, 339–361.
Raabe, D., Wang, Y., Roters, F., 2005. Crystal plasticity simulation study on the influence of texture on earing in steel. Computational Materials Science 34, 221–234.
Ray, R.K., Jonas, J.J., Hook, R.E., 1994. Cold rolling and annealing textures in low carbon and extra low carbon steels. International Materials Reviews 39, 129–172.
Senuma, T., Kawasaki, K., 1994. Texture formation in Ti-bearing IF steel sheets throughout the rolling and annealing processes in terms of the influence of hot rolling conditions on deep drawability. ISIJ International 34, 51–60.
Tikhovskiy, I., Raabe, D., Roters, F., 2007. Simulation of earing during deep drawing of an Al–3% Mg alloy (AA 5754) using a texture component crystal plasticity FEM. Journal of Materials Processing Technology 183, 169–175.
Tikhovskiy, I., Raabe, D., Roters, F., 2008. Simulation of earing of a 17% Cr stainless steel considering texture gradients. Materials Science and Engineering A 488, 482–490.
Yoon, J.W., Dick, R.E., Barlat, F., 2011. A new analytical theory for earing generated from anisotropic plasticity. International Journal of Plasticity 27, 1165–1184.
Zhao, Z., Mao, W., Roters, F., Raabe, D., 2004. A texture optimization study for minimum earing in aluminum by use of a texture component crystal plasticity finite element method. Acta Materialia 52, 1003–1012.